Astronomical Techniques and Instruments, Vol. 2, November 2025, 358–365

Article Open Access

Performance analysis and strategy optimization of mechanical defrosting for an Antarctic near-infrared telescope using aperture photometry

Jiali Chen[1,2,3], Zhengyang Li[1,2,4*], Zhixu Wu[5*], Jia'nan Cong[1,2,3], Zichong Zhang[6,7], Kaiwen Zheng[1,2,3]

[1]*Nanjing Institute of Astronomical Optics & Technology*, *Chinese Academy of Sciences*, *Nanjing* 210042, *China*

[2]*CAS Key Laboratory of Astronomical Optics & Technology*, *Nanjing Institute of Astronomical Optics & Technology*, *Nanjing* 210042, *China*

[3]*University of Chinese Academy of Sciences*, *Beijing* 100049,*China*

[4]*Polar Research Institute of China*, *Shanghai* 200136, *China*

[5]*Nanchang University*, *Nanchang* 330031, *China*

[6]*School of Astronomy and Space Science*, *Nanjing University*, *Nanjing* 210093, *China*

[7]*Key Laboratory of Modern Astronomy and Astrophysics*, *Nanjing University*, *Nanjing* 210093, *China*

*Correspondences: zyli@niaot.ac.cn; wuzhixu@ncu.edu.cn

Received: June 30, 2025; Accepted: August 5, 2025; Published Online: August 6, 2025; https://doi.org/10.3724/ati2025057; https://cstr.cn/32083.14.ati2025057

Citation: Chen, J. L., Li, Z. Y., Wu, Z. X., et al. 2025. Performance analysis and strategy optimization of mechanical defrosting for an Antarctic near-infrared telescope using aperture photometry. *Astronomical Techniques and Instruments*, **2**(6): 358−365. https://doi.org/10.3724/ati2025057.

Abstract: Dome A, in Antarctica, offers an exceptional site for ground-based infrared astronomy, with its extremely low atmospheric infrared background noise and excellent seeing conditions. However, deploying near-infrared telescopes in the harsh environment of Antarctica faces the critical challenge of frost accumulation on optical mirrors. While indium tin oxide heating films effectively defrost visible-band Antarctic astronomical telescopes, their thermal radiation at infrared wavelengths introduces significant stray light, severely degrading the signal-to-noise ratio for infrared observations. To address this limitation, we have designed a mechanical snow-removal system capable of efficiently clearing frost from sealing window surfaces at temperatures as low as –80°C. Aperture photometry of target sources, Canopus and HD 2151, revealed that after six days without intervention, floating snow extinction reduced target brightness by up to 3 magnitudes. Following mechanical defrosting, the source flux recovered to stable levels, with measured magnitudes showing rapid initial improvement followed by stabilization. Data analysis indicates that a frost removal strategy operating every 48 h, with each operation consisting of 4–6 cycles, enables efficient removal of frost and snow without introducing additional thermal noise. Future work will focus on optimizing the adaptive control algorithm and exploring novel low-temperature defrosting materials to extend the periods during which Antarctic infrared telescopes can operate unattended.

Keywords: Dome A; Antarctic infrared thermal radiation; Mechanical defrosting; Aperture photometry

1. INTRODUCTION

Infrared observations are capable of penetrating interstellar dust, and are extensively employed in astronomical research to probe protostellar evolution within star-forming regions, analyze the atmospheric composition of exoplanets, trace accretion processes in active galactic nuclei, and detect radiation signatures from high-redshift objects in the early universe. At typical astronomical sites, the performance of infrared telescopes in terms of survey depth, limiting magnitude, and exposure time of astronomical imaging systems is limited by near-infrared sky background radiation. Dome A in Antarctica possesses unique geographical advantages, with thin, dry air containing extremely low precipitable water vapor, high atmospheric transparency, and exceptional seeing conditions. Optical telescopes deployed at this site can achieve uninterrupted observations for 3–4 consecutive months, significantly improving observational efficiency[1]. With winter temperatures below −80°C at Dome A, thermal infrared back-

ground radiation shifts longward of 4 μm, with significant corresponding suppression of near-infrared sky background noise. A collaboration between a research team led by Dr. Jian Wang, from the University of Science and Technology of China, and the Astronomy Research Laboratory of the Polar Research Institute of China, has developed a near-infrared sky background measurement instrument for Antarctic observations. The instrument measures the intensity of the sky background at Dome A in Antarctica across the J, H, and Ks bands[2], with values ranging from 600–1 100 μJy arcsec^{-2}, 1 100–2 600 μJy arcsec^{-2}, and 200–900 μJy arcsec^{-2}. This demonstrates that Dome A in Antarctica, with its optimal visibility and geographical location, is regarded as the foremost site on Earth for far-infrared to submillimeter wave observations.

Antarctic optical and infrared telescopes typically have one or more exposed optical surfaces required to withstand the extreme environment. During Antarctic polar night, temperatures fall to −80°C, while the relative humidity level approaches 100%. When supersaturated air flows across optical surfaces below the frost point, direct deposition of water vapor occurs, forming frost layers on mirrors[3]. Frost accumulation significantly reduces mirror transmittance, severely diminishing telescope efficiency. Uneven frost deposition induces random phase fluctuations, amplifies scattered light, and introduces image distortion, collectively degrading optical resolution and image quality. Critically, frost contamination compromises data integrity by impairing high-precision photometric and spectroscopic measurements, which is particularly detrimental for frontier investigations of dark matter and exoplanets that rely on high-sensitivity measurements. To address this issue, the Nanjing Institute of Astronomy Optics & Technology (NIAOT), Chinese Academy of Sciences, developed anti-frost technology for Indium Tin Oxide (ITO) film coatings on astronomical telescope mirrors. This technology was first successfully implemented on the Chinese Small Telescope Array (CSTAR), at Kunlun Station in Antarctica (located approximately 7.3 km southwest of Dome A, at an altitude of 4 087 m), in January 2008[4], and has since been adopted for use on the Antarctic Survey Telescope (AST3-1, AST3-2, and AST3-3) and space debris telescopes.

However, for Antarctic infrared telescopes, ITO-based mirror defrosting introduces additional infrared thermal radiation at the optical pupil plane. This thermal radiation generates isoplanatic stray light across the entire field of view, which cannot be mitigated through conventional baffling or absorption techniques, ultimately degrading observational contrast and sensitivity. Furthermore, conditions at Kunlun Station are currently not equipped for personnel to overwinter, preventing manual intervention to remove frost and snow from the mirror surface. To enable the removal or reduction of frost and snow accumulation on the mirror surface of Antarctic telescopes and mitigate loss of light transmission or reflectivity, and to overcome the challenge of thermal noise from conventional heating-based defrosting methods, we present a mechanical snow-removal device and a fully automated mechanical de-icing method specifically designed for the first near-infrared telescope in Antarctica. These systems facilitate the efficient clearance of loose surface snow from the sealing window at temperatures as low as −80°C while maintaining observation quality. In this paper, we first establish a thermal radiation model for ITO heating and de-icing, in which the sealing window has a circular temperature distribution. This model is combined with the Stefan-Boltzmann law to quantitatively analyze the infrared thermal radiation emitted by mirror heating. Subsequently, we analyze photometric data acquired by the Antarctic 15 cm Near Infrared Telescope (15-NIRT) operating under mechanical de-icing. We conduct continuous observations of the target sources Canopus and HD 2151 using aperture photometry and analyze the extinction ratios of these targets at different snow removal and de-icing frequencies, along with trends in their apparent magnitudes. Finally, based on the analysis results, we optimize the mechanical de-icing strategy to minimize any potential impact on telescope operation.

2. ANALYSIS OF THERMAL RADIATION FOR HEATED SEALING WINDOW DEFROSTING

2.1. ITO Heating Defrosting Principle

ITO is a functional thin-film material composed of 90% indium oxide (In_2O_3) and 10% tin oxide (SnO_2). In optoelectronics, ITO functions as a thin-film material with a wide bandgap, ranging from 3.5 to 4.3 eV. Because of its high carrier concentration and electron mobility, ITO exhibits low resistivity, reaching levels as low as 10^{-4} Ωcm, and demonstrates excellent electrical conductivity[5]. Consequently, de-icing approaches using ITO-coated mirrors, coupled with electrode heating, have been investigated[6,7]. Fig. 1 shows the frosting issue encountered during the operation of AST3-2 in the extreme environment of Antarctica. The results confirm that a combination of ITO coating and electrode heating can effectively clear frost and snow from the window surface.

Early implementations of ITO-based de-icing employed direct current (DC) heating with point electrodes. These electrodes were significantly smaller than the mirror surface area, and de-icing was achieved by applying a fixed voltage difference between the positive and negative terminals. However, in this method, the current is localized near the electrodes, causing reduced current density in regions distant from the electrodes and consequently resulting in heterogeneous temperatures across the mirror surface. This consequent heterogeneous temperature distribution causes non-uniform thermal expansion across the mirror surface, inducing turbulence effects near the window. These temperature variations not only degrade the optical imaging quality but also reduce the imaging resolution. To address this, Zheng et al. proposed a method of de-

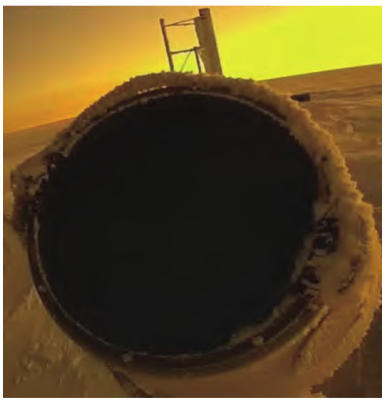

Fig. 1. The defrosting effect on the AST3-2 sealing window, showing a clear circular surface in the center and a visible accumulation of frost and snow along the edges.

icing using multi-phase alternating current (AC), combined with linear electrodes. Their experiments demonstrated an 81.61% reduction in the standard deviation of the mirror temperature and a 76.31% reduction in the peak-to-valley value, significantly improving heating uniformity and de-icing efficiency[6].

2.2. Thermal Radiation Effects on Near-infrared Telescope Sealing Window

"Stray light" refers to unwanted light in an optical system, comprising both non-target radiation scattered onto the detector or imaging surface and target radiation reaching the detector via paths not intended in the design of the instrument. Stray light degrades image plane contrast and the modulation transfer function (MTF), leading to reduced tonal range, degraded sharpness, and perturbed energy distribution. It can also generate spurious spots on the image plane or saturate the target signal entirely with stray radiation-induced noise. For infrared systems operating during polar night, the dominant sources of stray light are moonlight, sky background radiation, and intrinsic thermal emission from the system itself. As the impact of moonlight can be mitigated by reorienting the telescope, this analysis focuses on sky background radiation and system thermal emission under moonless conditions. The sky background illuminance $E_{\rm sky}$, on the telescope image plane is given by

$$E_{\rm sky} = \frac{I\left(\dfrac{c}{\lambda_1} - \dfrac{c}{\lambda_2}\right)\cdot fov}{10^6 \times 10^{26}} \times \frac{\pi R^2 \tau}{S}, \tag{1}$$

where c = 2.9979 × 10^8 m s^{-1} is the speed of light, λ_1 and λ_2 are the endpoints of the band range, I is the background brightness of the sky, fov = 7.903 × 10^6 arcsec^2 is the field of view of the telescope, and R = 0.075 m is the radius of the pupil. The efficiency of the telescope system is τ = 78.73%, and the camera sensor area is S = 3.277 × 10^{-5} m^2.

During the Antarctic winter, the sky background flux in the J, H, and Ks bands is approximately 600–1 100 μJy arcsec^{-2}, 1 100–2 600 μJy arcsec^{-2} and 200–900 μJy arcsec^{-2}, respectively. For the corresponding bands, we take the sky background intensities to be $I_{\rm J}$ = 600 μJy arcsec^{-2}, $I_{\rm H}$ = 1 100 μJy arcsec^{-2}, and $I_{\rm Ks}$ = 200 μJy arcsec^{-2}. The resulting image plane illuminances, calculated using Equation (1) for each band, are given in Table 1.

Table 1. Illumination of the sky background to the image plane in the J, H, and Ks bands

Waveband	Wavelength/μm	Illumination, $E_{\rm sky}$/(W m^{-2})
J	1.1–1.4	1.1765 × 10^{-6}
H	1.5–1.8	1.2302 × 10^{-6}
Ks	2.0–2.3	1.3129 × 10^{-7}

Emissivity is one of the main parameters in analyzing thermal radiation from infrared optics. According to the Stefan-Boltzmann law, the intensity of thermal radiation is proportional to the fourth power of temperature, where the radiance, j^* in W m^{-2}, is given by

$$j^* = \varepsilon \sigma T^4, \tag{2}$$

where ε is the blackbody radiance coefficient, which is equal to 1 for an absolute blackbody, and T is the absolute temperature in Kelvins. The scaling factor, σ, is the Stefan-Boltzmann constant, given by

$$\sigma = \frac{2\pi^5 k^4}{15c^2h^3} = 5.66 \times 10^{-8}\ \text{W m}^{-2}\ \text{K}^{-4}, \tag{3}$$

where k is Boltzmann's constant (1.380 649 × 10^{-23} J K^{-1}), and h is Planck's constant (6.626 07 × 10^{-34} J s). According to Planck's law of blackbody radiation, the radiative power per unit wavelength per unit volume can be expressed as

$$u(\lambda, T) = \frac{2\pi hc}{\lambda^5} \frac{1}{e^{hc/\lambda KT} - 1}. \tag{4}$$

Using Planck's law, we calculate the spectral radiance curves for an ideal blackbody at a range of temperatures. These curves represent the total electromagnetic power radiated per unit area, per unit solid angle, per unit wavelength. Fig. 2 shows the spectral distribution of blackbody radiance. At −60°C, the J-band spectral radiance remains below 0.1 W m^{-2} μm. However, when the temperature rises to −40°C, this radiance increases to approximately 10 W m^{-2} μm, representing an enhancement of nearly two orders of magnitude. Thermal radiation effects consequently become non-negligible. At longer wavelengths in the near-infrared H and K bands, blackbody radiance intensifies significantly. Particularly in the K band, spectral radiance exceeds 10^3 W m^{-2} μm even at −80°C, posing considerable challenges for proposed Antarctic K-band infrared optics.

For infrared systems, the energy of infrared radiation can be calculated using Planck's formula,

$$M = \varepsilon \int_{\lambda_1}^{\lambda_2} \frac{2\pi hc}{\lambda^5} \frac{1}{e^{hc/\lambda KT} - 1} \mathrm{d}\lambda, \tag{5}$$

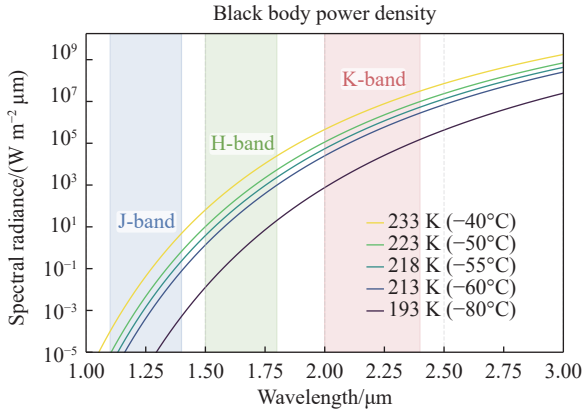

Fig. 2. Energy density of blackbody radiation at different wavelengths and temperatures.

where λ_1 and λ_2 correspond to the respective wavelength bands, and ε is the emissivity. The radiance of each surface in the optical system can therefore be calculated at different wavelengths.

Thermal radiation analysis was performed on the actual optomechanical system using 15-NIRT. With the ambient temperature set to −60°C (213.15 K) and the sensor detection range spanning 0.4–1.7 μm, we analyzed thermal radiation across four spectral bands (0.4–1.1 μm, 1.1–1.4 μm, 1.4–1.7 μm, and 1.7–2.5 μm) to inform the K-band optical design. Given that the filter coating functions as an anti-reflection layer in the 1.1–1.4 μm band, while acting as a reflector in the other three bands, the resulting radiant exitance values for each optical surface configuration are given in Table 2.

Table 2. Thermal radiation characteristics of component surfaces

Surface type	Temperature/°C	Emissivity	Wavelength/μm
Mirror	−60	0.03	0.4–1.1 1.1–1.4 1.4–1.7 1.7–2.5
Anti reflect	−60	0.002	0.4–1.1 1.1–1.4 1.4–1.7 1.7–2.5
Black paint	−60	0.95	0.4–1.1 1.1–1.4 1.4–1.7 1.7–2.5
Filter	[−58, −40]	0.03 0.002 0.03 0.03	0.4–1.1 1.1–1.4 1.4–1.7 1.7–2.5

The sealing window temperature decreases gradually from −40°C externally to −58°C internally, simulating the resulting uneven temperature distribution caused by heating. We conducted a radiant emittance analysis with TracePro ray tracing software, using the surface optical properties detailed in Table 3. Fig. 3 shows the ray tracing of optical-mechanical thermal radiation, and Table 4 shows the irradiance of thermal radiation on the imaging plane at different wavelengths.

Table 3. Optical characteristics of component surfaces

Surface type	Absorptance	Specular reflectance	Specular transmittance	Integrated BRDF*	BRDF A	BRDF B	BRDF g	Integrated BTDF**	BTDF A	BTDF B	BTDF g
Mirror	3×10^{-2}	9.5×10^{-1}	0	1×10^{-4}	7×10^{-6}	1×10^{-2}	2	0	0	0.1	0
Anti reflect	1×10^{-3}	1.5×10^{-2}	0.984	1.324×10^{-4}	1×10^{-5}	1.5×10^{-2}	2	7.53×10^{-5}	1×10^{-5}	0.1	2
Black paint	9.5×10^{-1}	1×10^{-5}	0	5×10^{-2}	1.9×10^{-2}	1	0	0	0	0.1	0

*BRDF: Bidirectional Reflectance Distribution Function; **BTDF: Bidirectional Transmittance Distribution Function.

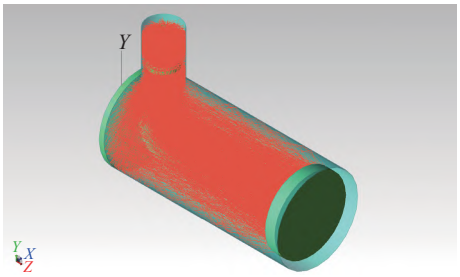

Fig. 3. Ray-tracing of opto-mechanical thermal radiation. The light green model shows the relative positions of the opto-mechanical components in the telescope system, while the orange rays represent the thermal radiation emitted by each component, reaching the imaging plane.

At the ambient temperature of –60 °C, the maximum irradiance on the image plane from optomechanical thermal radiation within the 0.4–1.7 μm band is 4.1868×10^{-12} W m^{-2}, which is substantially lower than sky background contributions. Consequently, thermal radiation negligibly affects imaging quality in the J and H bands. However, within the 1.7–2.5 μm band, thermal irradiance reaches 4.2096×10^{-7} W m^{-2}, comparable to K-band sky background levels, which compromises imaging quality. This thermal influence is projected to intensify further at longer mid-infrared wavelengths, meaning that ITO mirror heating becomes unsuitable for normal system operation in the K-band and longer wavelengths regimes.

2.3. Other Effects of ITO Heating Defrosting

Beyond the imaging effects of thermal radiation generated by ITO electrode heating, the near-infrared transmittance of ITO coatings also impacts optical performance. While ITO has 85% transmittance at visible wavelengths, it shows significant reflection in near-infrared bands, caused by carrier plasmon oscillations[7], and increased film thickness further exacerbates scattering and absorption losses. These properties are characterized by the Drude model for ITO materials[8].

Table 4. Image plane irradiance

Wavelength/μm	Irradiance/(W m^{-2})
0.4–1.1	5.8737×10^{-21}
1.1–1.4	1.4917×10^{-15}
1.4–1.7	4.1868×10^{-12}
1.7–2.5	4.2096×10^{-7}

The material permittivity, $\varepsilon(\omega)$, is given by

$$\varepsilon(\omega) = \varepsilon_\infty - \frac{\omega_p^2}{\omega^2 + i\omega\gamma} = \varepsilon_1 + i\varepsilon_2, \tag{6}$$

where ε_∞ is the high frequency permittivity, ω is the angular frequency, ω_p is the plasma frequency, and γ is the damping rate. The real part (ε_1) and imaginary part (ε_2) of the permittivity are given by

$$\varepsilon_1 = \varepsilon_\infty - \frac{\omega_p^2}{\omega^2 + \gamma}, \tag{7}$$

and

$$\varepsilon_2 = \frac{\gamma\omega_p^2}{\omega(\omega^2 + \gamma^2)}. \tag{8}$$

The complex refractive index, $\tilde{n}$, is given by

$$\tilde{n}^2 = (n + ik)^2, \tag{9}$$

where n is the ordinary refractive index, and k is the extinction coefficient, which are given, respectively, by

$$n = \sqrt{\frac{\sqrt{\varepsilon_1^2 + \varepsilon_2^2} + \varepsilon_1}{2}} \tag{10}$$

and

$$k = \sqrt{\frac{\sqrt{\varepsilon_1^2 + \varepsilon_2^2} - \varepsilon_1}{2}}. \tag{11}$$

According to Fabry-Perot interference theory, the total field amplitude is given by

$$r = \frac{r_{01} + r_{10}e^{i2\phi}}{1 + r_{01}r_{10}e^{i2\phi}} \tag{12}$$

and

$$t = \frac{t_{01}t_{10}e^{i2\phi}}{1 + r_{01}r_{10}e^{i2\phi}}, \tag{13}$$

where r is the total reflection amplitude coefficient, t is the total transmission amplitude coefficient, r_{ij} is the amplitude reflection coefficient, t_{ij} is the amplitude transmission coefficient, e is the natural exponential, and ϕ is the single-pass phase accumulation during light propagation through the thin film. These coefficients satisfy the Stokes relation $t_{ij}t_{ji} + r_{ij}^2 = 1$. The coefficients are calculated using the relationships

$$r_{01} = \frac{\tilde{n} - 1}{\tilde{n} + 1},\ t_{01} = \frac{2}{\tilde{n} + 1}, \tag{14}$$

$$r_{10} = \frac{1 - \tilde{n}}{1 + \tilde{n}},\ t_{10} = \frac{2\tilde{n}}{\tilde{n} + 1}, \tag{15}$$

and

$$\phi = \frac{2\pi}{\lambda}\tilde{n}d, \tag{16}$$

where λ is the corresponding wavelength and d is the film thickness. Derivations of the formula for the calculation of the ITO film curve parameters can be obtained from Equation (14) and Equation (15), as

$$R = |r|^2,\ T = |t|^2, \tag{17}$$

and

$$A = 1 - R - T, \tag{18}$$

where R is the reflectance of the ITO thin film corresponding to the thickness as a function of wavelength, T is the transmittance, and A is the absorptance. For a thickness of 0.2 μm[9], we used Python to calculate spectra for T, R, and A across the 0.4–3 μm range (shown in Fig. 4). For wavelengths further into the infrared, ITO transmittance decreases progressively, maintaining 70%–75% in the J-band, dropping to a minimum of 40% in the H-band, and falling to only 20%–30% in the K-band. This severe attenuation fundamentally compromises infrared light collection efficiency. Consequently, ITO-coated electrode heating is unsuitable for de-icing sealing windows on near-infrared telescopes.

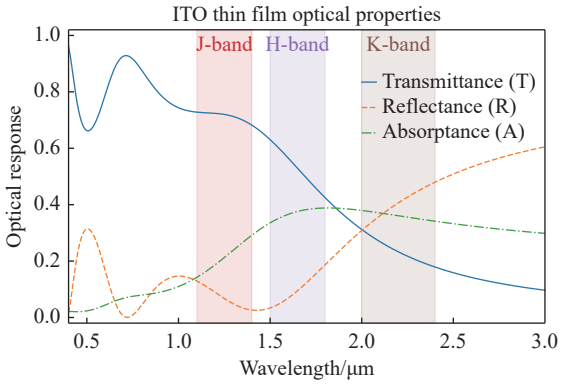

Fig. 4. Transmittance, absorptance, and reflectance curves of ITO in the 0.4–3 μm wavelength range.

3. PERFORMANCE ANALYSIS OF MECHANICAL SNOW REMOVAL AND DEFROSTING

3.1. Design of a Device for Mechanical Snow Removal

The performance of the snow removal system was

tested on 15-NIRT. The telescope uses a modified hyperbolic Newtonian optical design, and compensates for spherical aberration and coma using a hyperbolic primary mirror and a corrector lens group, achieving excellent image quality and a wide field of view. For a fully enclosed mechanical structure, protecting the instrument interior from wind-blown snow and ice (which could degrade imaging performance and shorten equipment lifespan), a sealing window is incorporated into the optical system. Made from fused silica, the sealing window incorporates a J-band filter coating on its surface, defining the operational wavelength range as 1.1–1.4 μm[10].

The snow-removal device was upgraded and installed on the near-infrared telescope by Dr. Chao Chen (NIAOT) during China's 41st Antarctic Research Expedition, in 2024. As shown in Fig. 5B, the device is mounted on the right side of the sealing window. It can be remotely controlled to initiate and terminate operation. The brush bristles possess moderate hardness, enabling effective snow removal while preventing damage to the filter coating of the sealing window.

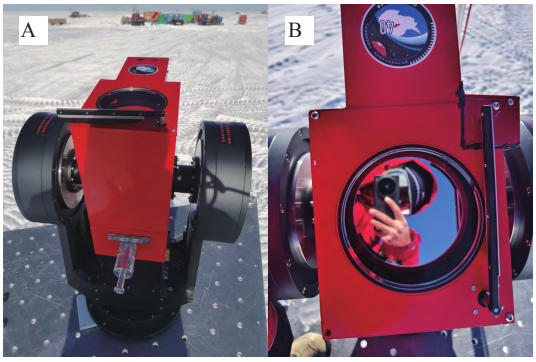

Fig. 5. (A) Near-infrared telescope snow brush at Dome A, Antarctica. (B) The snow removal device.

3.2. Mechanical Defrosting Performance Evaluation Method

Currently, no suitable sensor is available to detect frost formation on optical mirror surfaces without compromising astronomical observations. Consequently, we have no way to visually monitor the effectiveness of the mechanical de-icing. Here, we propose quantifying the effectiveness of mechanical de-icing through aperture photometry. Aperture photometry is a fundamental technique in astronomical image analysis for measuring the brightness of celestial objects, such as stars or galaxies. It involves measuring the flux within a small aperture region defined by the focal plane diaphragm or image-processing software. The source intensity is calculated by summing the counts within the aperture containing the source and subtracting the estimated sky background contribution derived from nearby image regions.

Aperture photometry employs spatial segmentation to isolate the light signal from the target celestial object from any surrounding background contribution (e.g., atmospheric glow). The inner aperture defines a region encompassing the target, collecting the total flux (source and local background). The aperture size critically affects the measurement: An excessively large aperture increases background noise, while an overly small aperture leads to source signal loss. The outer aperture measures the local background intensity, typically chosen as an annulus surrounding the inner aperture or as discrete regions nearby. This selection aims to minimize distance to the target while avoiding contamination from the its halo or any neighboring celestial objects. When the stellar Point Spread Function (PSF) extends beyond the aperture, the resulting flux loss necessitates aperture correction of the instrumental magnitude. The correction formula, calculating the aperture correction value, $\Delta m'$, is

$$\Delta m' = m_{\mathrm{B}} - m_{\mathrm{S}}, \tag{19}$$

where m_{B} and m_{S} are the large and small apertures of bright stars, respectively. The large aperture is usually several times larger than the small aperture, covering almost the entire target source flux, while the small aperture is consistent with the dark star photometric aperture. When a star is well-isolated within the stellar field, its photometric value can be measured using aperture photometry (as illustrated in Fig. 6). The fundamental steps are as follows[11]:

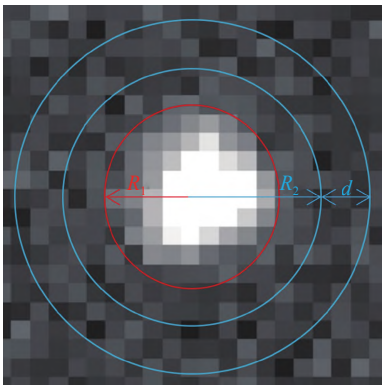

Fig. 6. Aperture photometry. The circle with radius R_1 is the photometric aperture. The circular ring, with a thickness of d, starting at the radius R_2, is used to calculate the sky background.

(1) Pre-processing (subtracting background and dark current, removing flat field);

(2) Searching for the target source;

(3) Determine the center of the star image in the given aperture, N_{a} pixels;

(4) Confirm the background value B of the sky light near the aperture;

(5) The total intensity, F_{a}, obtained by adding up all the pixel values that fall within the aperture;

(6) Calculate the size of celestial objects, $m' = -2.5 \log [F_{\mathrm{a}} - N_{\mathrm{a}} \times B]$;

(7) Performing aperture correction $\Delta m'$;

(8) Obtain the magnitude of the instrument $m = m' + \Delta m'$.

3.3. Quantitative Analysis of Mechanical Defrosting Effectiveness

Observations of the target star Canopus were obtained at UTC 2025−03−05 T13:38:27 and UTC 2025−03−11 T13:33:18, each with a 0.1 s exposure. We performed data analysis using the MaxIm DL 6 software package. After six days without snow removal, accumulated frost/snow attenuates the target flux by approximately 3 magnitudes, severely degrading the observational data quality (see Fig. 7).

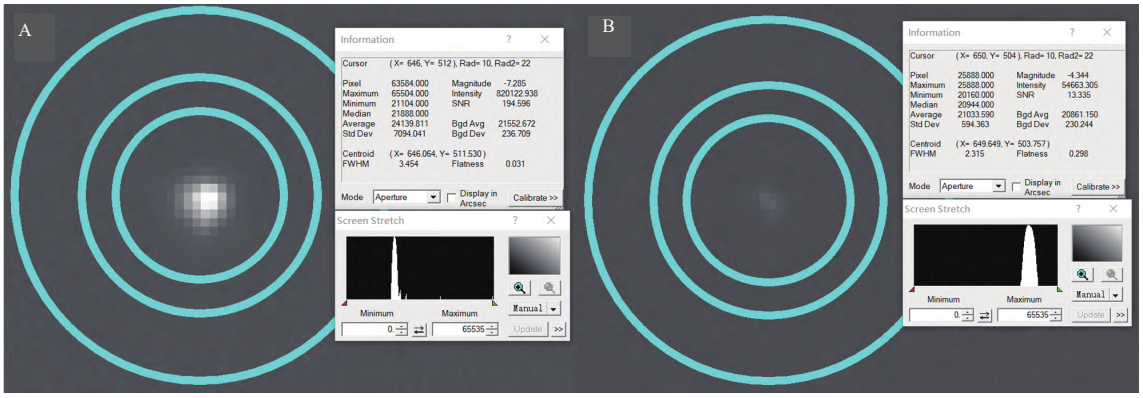

Fig. 7. Canopus observations performed on (A) UTC 2025−03−05 T13:38:27 and (B) UTC 2025−03−11 T13:33:18. The blue circles show the aperture photometry regions. The white text boxes display key image parameters, including the maximum and minimum pixel values, magnitude, and Full Width at Half Maximum (FWHM).

Prior to each observing session, a reference image was acquired for each target. Following each snow removal operation, the target was exposed identically. Approximately 15 images were obtained per target, with the entire sequence completed within 30 minutes, to minimize atmospheric turbulence effects on photometry. The targets selected were Canopus and HD 2151. To maximize snow accumulation effects, no snow removal was performed for 3 days preceding the Canopus observation. HD 2151 was observed one day after Canopus to evaluate 24-hour snow accumulation changes. Both targets were exposed for 0.1 s. Data were processed and analyzed using Python. Initial steps included error correction by subtracting bias and dark current, and applying flat-field correction. Flux measurements were then performed on the corrected images. Magnitude analysis used the derived flux data. The first image served as the reference. We calculated the magnitude difference between each post-snow-removal measurement and the pre-snow-removal reference magnitude, and the resulting flux and magnitude variations are shown in Fig. 8.

Fig. 8A shows the variation in target flux. As snow removal operations increase, the target flux initially rises and then stabilizes, providing preliminary evidence for the effectiveness of the device in mitigating the effects of accumulated snow and frost. Fig. 8B shows the relative magnitude change of the target before and after snow removal, calculated by subtracting the magnitude measured without snow removal from that measured after snow removal. Under identical exposure times, we observed an increase in target brightness, which aligns with the expected performance of the snow removal device.

Further analysis reveals that after 3 days without snow removal, Canopus showed a change of approximately 1 magnitude. By contrast, HD 2151, observed only 1 day after its previous snow removal, showed a much smaller relative magnitude change of ~0.2 magnitudes. This indicates that the impact of snow accumulation on observations increases with time since the last removal. The data also show that magnitude changes saturate after approximately 5 snow removal cycles. Based on

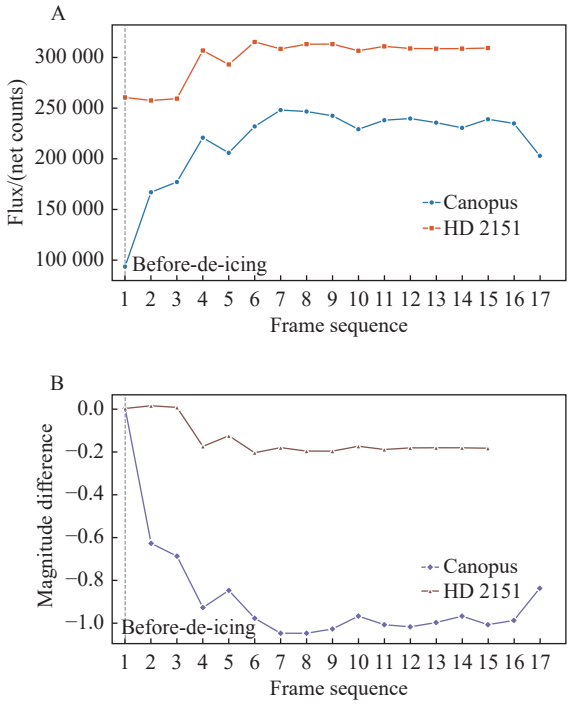

Fig. 8. Variation in data for Canopus and HD 2151 as a function of increasing snow removal cycles. (A) shows the variation in target flux, while (B) displays the relative magnitude variation.

these results, we suggest optimizing the snow removal frequency to around 48 h, with each session comprising 4–6 cycles, for operational efficiency.

4. CONCLUSION

We have evaluated the effectiveness of a mechanical snow removal device using 15-NIRT at Dome A, in Antarctica. We first analyzed the performance of heating using ITO coatings for defrosting, then examined its limitations for near-infrared applications, including thermal radiation from sealing window heating and reduced transmittance of ITO films in the NIR band. We used changes in target flux and magnitude before and after snow removal to perform a quantitative analysis. Approximately 15 exposures were acquired for each target (Canopus and HD 2151), with the total sequence completed within 30 min to minimize atmospheric turbulence effects. Data were processed using Python. The results align with the expected performance of the device. Target flux increased and stabilized with successive snow removal operations, and the relative magnitude change peaked and then plateaued, consistently reaching its maximum during the 5^{th} to 6^{th} cycle. Considering snow removal intervals of 1–3 days, we recommend an optimized regimen of snow removal at 48-hour intervals, with each session comprising 4–6 cycles. This approach provides a straightforward but effective solution for removing accumulated snow and frost from the sealing window, significantly improving observational efficiency.

ACKNOWLEDGEMENTS

This work was supported by the Space Debris Research Project, China (KJSP2020010102), the National Key R&D Program of China (2022YFC2807300), and the National Natural Science Foundation of China (12573081).

AI DISCLOSURE STATEMENT

Deepseek was employed for code error checking during the calculations in this paper and for language and grammar checking of the article. The authors carefully reviewed, edited, and revised the Deepseek-generated texts to their own preferences, assuming ultimate responsibility for the content of the publication.

AUTHOR CONTRIBUTION

Zhengyang Li and Zhixu Wu supervised the project, contributed to conceptualization and oversaw the technical workflow. Jiali Chen and Kaiwen Zheng acquired the observational data. Jia'nan Cong supervised and guided the thermal radiation analysis. Zichong Zhang performed data analysis and processing. Jiali Chen and Zhixu Wu drafted the manuscript and edited it for language. All authors read and approved the final manuscript.

DECLARATION OF INTERESTS

Zhengyang Li is an executive editor-in-chief for Astronomical Techniques and Instruments and he was not involved in the editorial review or the decision to publish this article. The authors declare no competing interests.

REFERENCES

[1] Lu, H. P., Yuan X. Y., Zhang K. Y. 2014. Infrared background radiation removing design and simulation of Antarctic survey telescope. *Acta Optica Sinica*, **34**(11): 1122002.

[2] Zhang, J., Zhang, Y. H., Tang, Q. J., et al. 2023. Sky-brightness measurements in J, H, and Ks bands at DOME A with NISBM and early results. *Monthly Notices of the Royal Astronomical Society*, **521**(4): 5624−5635.

[3] Du, F. J., Li, Z. Y., Yuan, X. Y. 2016. Chinese antarctic astronomical progression and expeditions. *Progress in Astronomy*, **34**: 43−50. (in Chinese)

[4] Yuan, X. Y., Cui X. Q., Liu, G. R., et al. 2008. Chinese Small Telescope Array (CSTAR) for Antarctic Dome A. In Proceedings of SPIE.

[5] Cheng, L. S., Sun, B. S., Zhong, J. M., et al. 2008. Development of ITO transparent and conductive thin films. *Rare Metals Letters*, **27**(3): 10−16. (in Chinese)

[6] Zheng, Y., Zhao, D., Yuan, X. Y., et al. 2015. Indium Tin Oxide thin films defrosting using multiphase AC design for Antarctic optical telescope. *Acta Optica Sinica*, **35**(6): 0631001.

[7] Wang, J. F., Wang, Y. R., Tian, J. 2017. Anti-frosting method for primary mirror film coating of large astronomical telescope in Antarctica. *Acta Optica Sinica*, **37** (4): 0431002.

[8] Nemati, A., Wang, Q., Hong, M. H., et al. 2018. Tunable and reconfigurable metasurfaces and metadevices. *Opto-Electronic Advances*, **1**(5): 18000901−18000925.

[9] Eshaghi, A., Graeli, A. 2014. Optical and electrical properties of indium tin oxide (ITO) nanostructured thin films deposited on polycarbonate substrates "thickness effect". *Optik*, **125**: 1478−1481.

[10] Li, Z. Y., Cong, J. N., Wu, Z. X., et al. 2024. System design for a wide field-of-view near-infrared telescope for Dome A in Antarctica. *Publications of the Astronomical Society of the Pacific*, **136**(11): 115002.

[11] Yang, G. P., Wu, W. T. 2012. Progressin the stellar CCD photometric methods. *Progress in Astronomy*, **30**(4): 467−486. (in Chinese)